

PANIC: a 3D dislocation dynamics model for climb and glide in epitaxial films and heterostructures

W. Y. Fu^{a,*}, C. J. Humphreys^a, M. A. Moram^{a,b}

^a*Dept. of Materials Science & Metallurgy, University of Cambridge, 27 Charles Babbage Road, Cambridge CB3 0FS, United Kingdom*

^b*Dept. of Materials, Imperial College London, Exhibition Rd., London SW7 2AZ, United Kingdom*

Abstract

This paper presents PANIC, a 3D discrete mesoscale dislocation dynamics model which includes a fully quantitative treatment of both dislocation climb and dislocation glide, including climb driven by both osmotic and mechanical stresses and climb enabled by both bulk and pipe diffusion, including full elastic anisotropy for materials with hexagonal symmetry. Efficient calculations can be performed for epitaxial thin films, multilayers and device structures with free surfaces, including those with irregular geometries (e.g. islands). The model also includes the capability to simulate dislocation dynamics during the growth of the thin films or heterostructures. The model has been validated against experiment for thin films of GaN, AlN and AlGaIn but is widely applicable to other material systems, both hexagonal and cubic.

Keywords: Dislocation dynamics, Plasticity, Thin films, III-V Semiconductors, GaN

1. Introduction

Dislocations are 1-dimensional line defects whose properties control the mechanical behaviour of many crystalline materials. Their existence was first proposed theoretically in 1934 by Taylor (1934), Orowan (1934a,b,c) and Polanyi (1934), while subsequent studies by Hirsch et al. (1956), Steeds (1973), Cottrell (1963), Hirth and Lothe (1982), and many others described the properties of dislocations, focusing their effects on the plasticity of metals. More recently, research in this area has included atomistic simulations of dislocation core structures (Belabbas et al., 2007;

*Corresponding author: Tel.: +44 (0)1223 334474.
Email address: wyf22@cam.ac.uk (W. Y. Fu)

Cserti et al., 1992; Fang and Wang, 2000) and dislocation mobilities (Olmsted et al., 2005; Weingarten and Chung, 2013), as well as mesoscopic dislocation dynamics simulations used to model the microstructural development of metals containing high densities of dislocations and subjected to stresses (von Blanckenhagen et al., 2004; Bulatov et al., 2004; Devincere et al., 2011; Ghoniem et al., 2000; Groh et al., 2003; Mordehai et al., 2008; Schwarz, 1999; Weygand et al., 2002; Zbib et al., 2001), and also multi-scale simulations spanning both atomistic and mesoscopic length scales (Bulatov et al., 1998). The majority of these simulations include dislocation glide, the rapid motion of dislocations within their slip plane in response to shear stresses acting across that plane. Dislocation climb can also occur, which is the non-conservative motion of dislocations perpendicular to their glide plane enabled by the diffusion of point defects towards or away from the dislocation core. However, the effects of dislocation climb are complex to calculate and greatly increase computational time. Earlier work includes dislocation climb as a simple 'drag factor' (Cai and Bulatov, 2004), and a bulk diffusion climb model has been properly introduced (Ghoniem et al., 2000; Mordehai et al., 2008). A full climb model has also been implemented recently in 2D by Ayas et al. (2014), but this is computationally too expensive for 3D simulations.

The behaviour of dislocations in semiconductors has received considerable attention, particularly in GaN-based materials where heteroepitaxial thin films and devices contain dislocation densities from $10^7 - 10^9 \text{ cm}^{-2}$. Dislocations in III-nitride devices are known to reduce device lifetimes (Furitsch et al., 2006; Mukai et al., 2006; Tapajna et al., 2011) and efficiencies (Khan et al., 2008; Zhu et al., 2013), as well as increasing leakage currents (Chan et al., 2009; Kaun et al., 2011). However, dislocations also affect the evolution of stresses during device growth. The high mismatch between the lattice parameters, thermal expansion coefficients and elastic constants of the III-nitride films and substrates mean that changes in epilayer composition or growth temperature are usually accompanied by changes in biaxial stresses. This is a major challenge for the growth of GaN-based devices on Si (Dadgar et al., 2000; Haerberlen et al., 2010; Krost and Dadgar, 2002; Zhu et al., 2013) and for AlGaN-based devices for ultraviolet light emitters (Amano et al., 1999; Han et al., 2001; McAleese et al., 2004), in which cracking frequently occurs due to the biaxial stresses generated during or after growth. Dopants (such as Si) may also interact with dislocations, further affecting the evolution of stresses during device growth. Previous studies have shown that Si-doping is associated with an increase in tensile stress in the film, but it tends to "pin" dislocations, limiting climb (Forghani et al., 2012; Moram et al., 2011a,b). There also appears to be a range of dislocation-mediated stress relaxation mechanisms in device structures: for instance, misfit dislocations are sometimes ob-

served in $\text{In}_x\text{Ga}_{1-x}\text{N}/\text{GaN}$ structures (Costa et al., 2005), while inclined dislocations (Chang et al., 2010) and “staircase” dislocations (Cherns et al., 2008) dominate in $\text{Al}_x\text{Ga}_{1-x}\text{N}/\text{GaN}$ structures. These devices are based on either c-axis oriented epitaxial films, or (more recently) other ‘nonpolar’ and ‘semipolar’ orientated films. In the former case, dislocation climb is an important mechanism for dislocation mobility (Fu et al., 2011; Moram et al., 2010) as the isotropic in-plane symmetry means that slip systems are rarely activated, despite the presence of high biaxial stresses. In the latter case, the loss of in-plane isotropy enables dislocation glide to occur in response to in-plane biaxial stress (Hsu et al., 2011, 2012). This can lead to extended dislocation segments forming inside the active region of nonpolar or semipolar devices, further reducing device performance.

A large body of literature is devoted to the behaviour of dislocations within III-nitride semiconductor devices but it has not yet been possible to predict the behaviour of dislocations quantitatively. In this work, we present a dislocation dynamics model which enables prediction of the dislocation microstructure in III-nitride films and devices, named PANIC (Parallel ANIsotropic dislocation Climb and glide). This model includes a full treatment of both climb and glide, combining mesoscopic dislocation mechanics with parameters derived from atomistic simulations of dislocation behaviour, and takes into account the effects of the anisotropic elasticity of nitride crystals, the effects of thin film or 3D patterned geometries and the influence of multi-layer image stresses, temperature changes, and the biaxial stresses arising from mismatches in lattice parameters, elastic constants and thermal expansion coefficients between different epilayers and/or the substrate. In short, it includes every parameter that could reasonably be expected to affect dislocation movement in III-nitrides. The model can also be applied to thin film processes including annealing and epitaxial lateral overgrowth (ELOG). Here, we describe the model and validate it by comparison to experimental data on the dislocation microstructure in thin films of GaN and AlGaN.

2. Methods

An overview of the approach used in this model is given in Fig. 1 and is outlined in detail in the following section.

2.1. *Simulation supercell*

The dislocation dynamics in III-nitride films and multilayers are modelled inside a cuboid anisotropic elastic space, which may include multiple layers of anisotropic elastic media. The dimensions L_x and L_y of the simulation space in the \mathbf{x} - and \mathbf{y} -

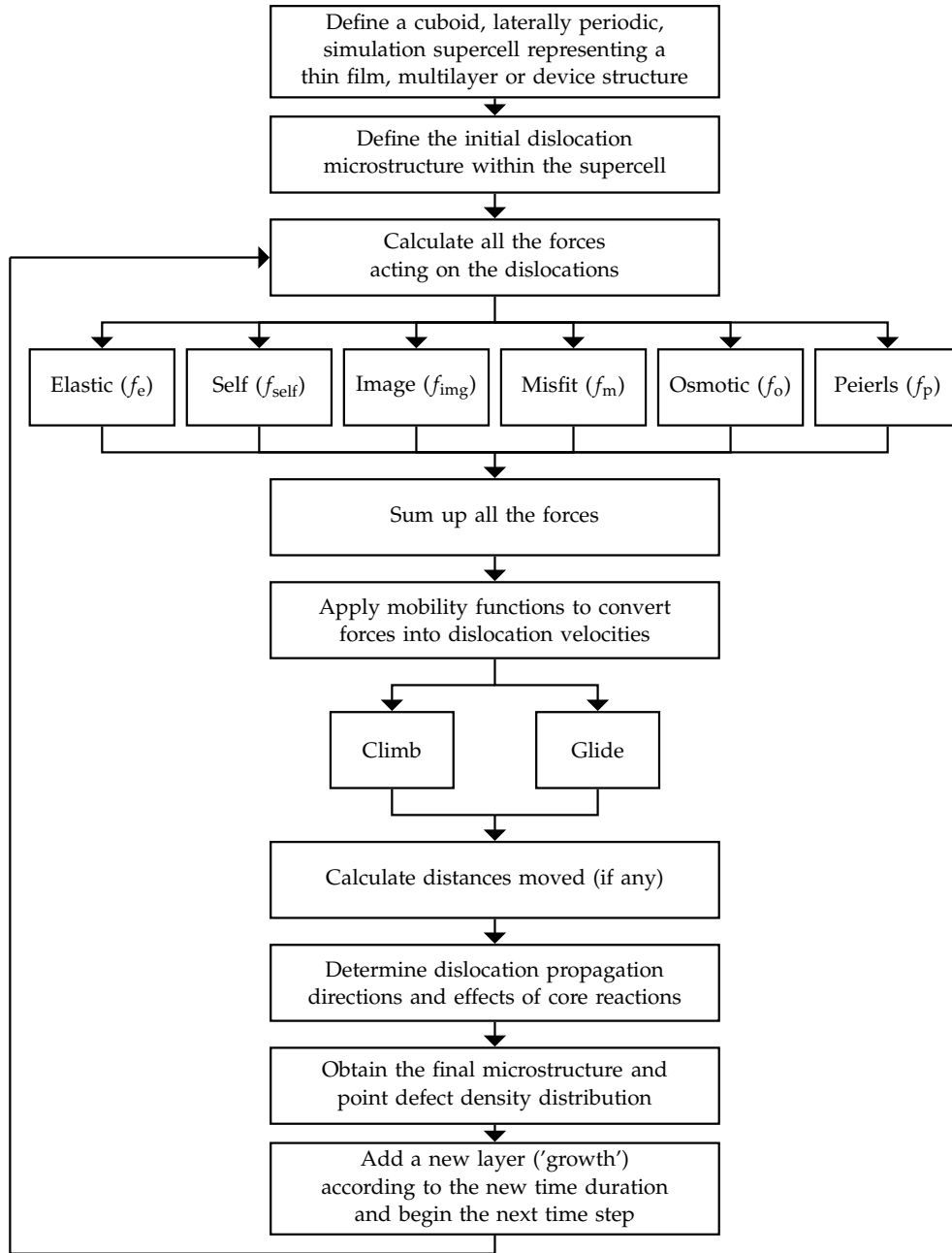


Figure 1: Flow chart illustrating the approach used in this discrete dislocation dynamics model.

Sample parameters	Material parameters
Dislocation density	Elasticity tensor \mathbf{C}
Number of (threading) dislocations in the simulation cell	Lattice parameters a and c
Ratio between \mathbf{c} -type, \mathbf{a} -type and $(\mathbf{a} + \mathbf{c})$ -type dislocations	Debye frequency ω_0
Thin film, multilayer or device structure and geometry	Dislocation core energy E_{core}
Crystallographic orientation of each layer	Temperature dependent thermal expansion function in the \mathbf{a} and \mathbf{c} directions
Temperature	Diffusion coefficients* for bulk diffusion D_B
External pressure	Glide activation energy Q_g
Growth rate	Pipe diffusion climb activation energy Q_p
Growth direction	Atomic volume

*includes the vacancy or interstitial formation energy, the diffusion coefficient pre-exponential factor and the self-diffusion enthalpy

Table 1: Input parameters required for the dislocation dynamics simulation.

directions are kept equal to facilitate the use of periodic boundary conditions, which help to emulate the effect of a large specimen or wafer on the local simulated region. Periodic boundary condition is not implemented in the \mathbf{z} - direction, however, so that the surface of the elastic space as well as the interface can be defined by one or more facet(s) which make up its geometry. Each layer in the simulation space is assumed to be crystalline and is allocated the properties summarised in Table 1.

The 4-index Miller-Bravais system is conventionally used to specify planes and vectors for hexagonal materials, however, it is more convenient to transform all 4-index vectors to Cartesian coordinates for geometric computation. This means that the simulation code can also be used for cubic materials. If the lattice vector $[2\bar{1}\bar{1}0]$ is parallel to the \mathbf{x} -axis and the lattice vector $[0001]$ is parallel to the \mathbf{z} -axis, then any lattice vector $[uvw]$ or reciprocal lattice vector $(hkil)$ of a hexagonal lattice system can be converted to the Cartesian coordinate system (x, y, z) using the following relations, where a and c are the lattice parameters of the hexagonal crystal:

$$[uvw] = \frac{3}{2}ua\mathbf{x} + \frac{\sqrt{3}}{2}(u + 2v)a\mathbf{y} + wc\mathbf{z} \quad (1)$$

$$(hkil) = \frac{h}{a}\mathbf{x} + \frac{h+2k}{\sqrt{3}a}\mathbf{y} + \frac{l}{c}\mathbf{z} \quad (2)$$

To account for semi-polar and non-polar film orientations, where the vector $[0001]$ is no longer aligned with the \mathbf{z} -axis, and for some films which may be deposited in a slightly different planar orientation with respect to the substrate, a coordinate orientation transformation is also implemented as described by Hirth and Lothe (1982), by applying a transformation matrix \mathbf{T} to the specific coordinate \mathbf{r} , with respect to the three Eulerian angles θ , ϕ and κ for transformation (see Fig. 2(a)). The stress $\boldsymbol{\sigma}$, strain $\boldsymbol{\epsilon}$ and stiffness tensor \mathbf{C} can thus be transformed using the transformation matrix accordingly (Hirth and Lothe, 1982).

2.2. Dislocation modelling

Pure dislocations in the III-nitrides can have any of the three possible Burgers vectors: $\frac{1}{3}\langle 11\bar{2}0 \rangle$ (\mathbf{a} -type), $\langle 0001 \rangle$ (\mathbf{c} -type) and $\frac{1}{3}\langle 11\bar{2}3 \rangle$ ($(\mathbf{a} + \mathbf{c})$ -type). Dislocations are first generated using positions and Burgers vectors assigned randomly using a Mersenne Twister algorithm (Matsumoto and Nishimura, 1998). For a typical simulation, each dislocation has a line vector $\boldsymbol{\xi}$ which is the same as the normal vector of the substrate plane, although manual setup of dislocation positions and orientations is also possible. The generated dislocations are then divided into small segments defined by positions of the two end nodes, so that segments with the same node are connected together. The minimum length of the dislocation segment is limited by the core radius of the dislocation and the magnitude of the error in the calculated dislocation movement arising from the time integration, while the maximum length is limited by the error related to the angle between two straight segments, which is proportional to the deviation from a long straight segment compared to a curved segment. This discretization allows freedom of movement of the dislocation line in each simulation step. At each time step, the segmentation of the dislocation is adaptively recalculated according to the above criteria and the angle between two segments, thus minimizing the computational power needed, while maintaining an acceptable spatial resolution.

2.3. Forces affecting dislocation movement

In this model, we consider and model the driving forces for the evolution of the dislocation microstructure existing in thin films under realistic growth conditions. At equally spaced points on each dislocation segment, the forces that are important to both glide and climb in multi-layered structures are calculated, including the elastic force, self-force, image force, misfit force, osmotic force and Peierls force. By integrating the points (using Simpson's rule) on a node's connected segments

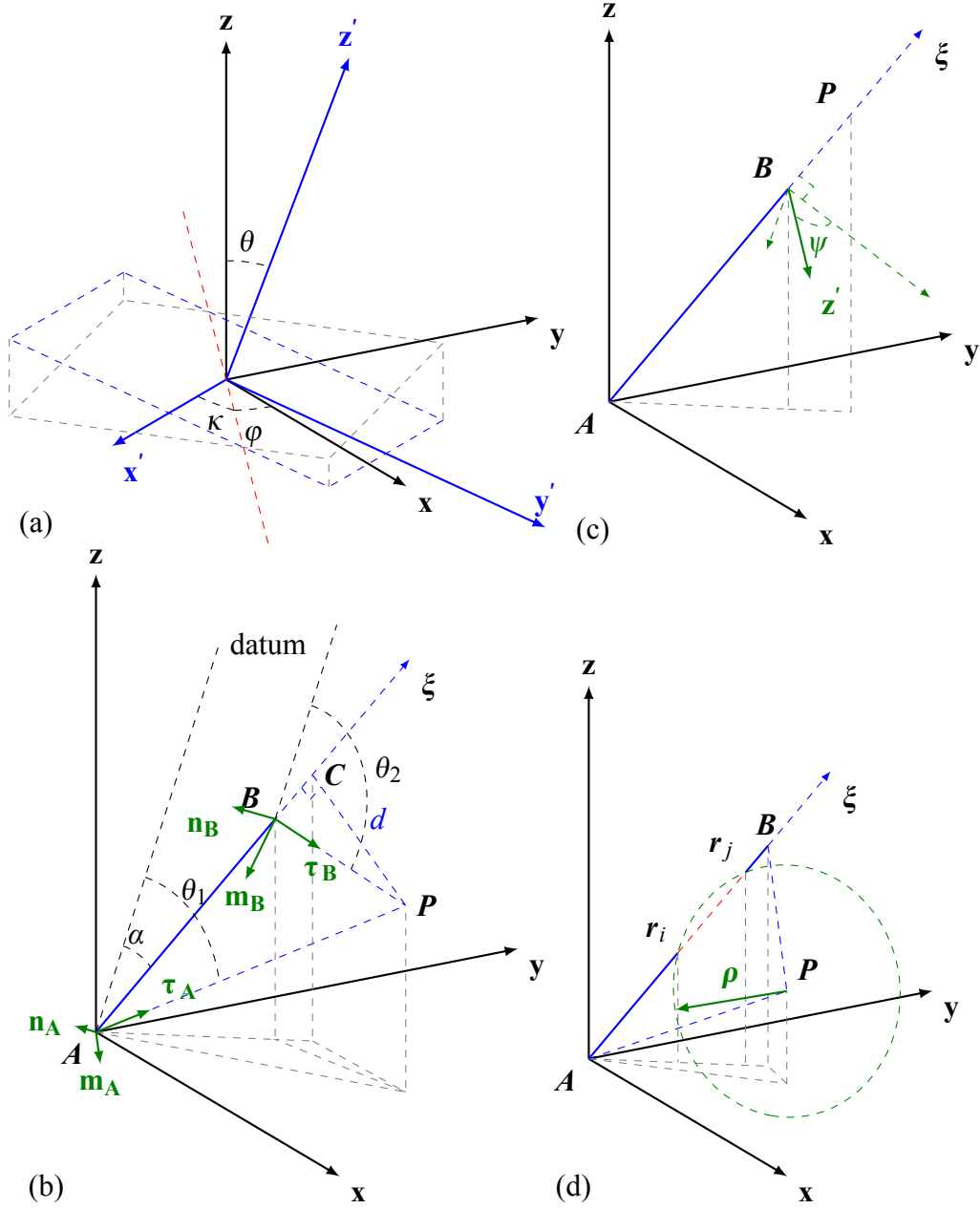


Figure 2: (a) The relationship between the hexagonal and the Cartesian coordinate axes used in this model; (b) The geometric illustration of the Willis-Steeds-Lothe equation (Eqn. 3) and Brown's equation (Brown, 1967); and geometric setup for (c) collinear field points and (d) field points within the core radius r_c of a dislocation segment.

with respect to a shape function, the segment now acts like it is pinned to the two nodes at its end points. The total integrated force can then be used to calculate the actual dislocation movement velocity using an adaptive 4th-5th order Adam-Bashforth-Moulton predictor corrector method (Mathews and Fink, 2006), with the first 3 time steps being initialized using the Euler-trapezoid method.

2.3.1. Elastic forces

The elastic interactions within and between dislocations are modelled by the cumulative effect of the computed stress fields from each dislocation on individual dislocation line segment. The summed stresses lead to an expression for the elastic force f_e per unit length L .

The initial method to calculate the stress field of a straight dislocation segment of finite length is proposed by Brown (1967) as a proof to the theorem of Lothe (1967), who expressed dislocation forces in terms of energy factors. However, this method causes singularity in collinear cases, thus we adopted the non-singular expression of Willis (1970), as described by Yin et al. (2010). This Willis-Steeds-Lothe formula describes the stress tensor field on a dislocation segment in an infinite anisotropic elastic space (using the Einstein summation convention):

$$\sigma_{ij}(\mathbf{r}) = \frac{1}{4\pi d} \epsilon_{qln} b_p C_{ijkl} C_{pqms} \xi_n \left\{ -m_s Q_{km} + n_s [(nn)^{-1} \cdot (nm) \cdot Q]_{km} + n_s [(nn)^{-1} \cdot S^T]_{km} \right\} \Big|_{\mathbf{AP}}^{\mathbf{BP}} \quad (3)$$

where σ is the stress tensor; ϵ is the permutation tensor; d is the distance $|\mathbf{CP}|$ from the dislocation line vector to the field point; C_{ijkl} is the component of the stiffness tensor $\mathbf{C}(\mathbf{r})$; \mathbf{b} is the Burgers vector; ξ is the dislocation line vector; \mathbf{m} , \mathbf{n} and $\boldsymbol{\tau}$ form an orthogonal basis as illustrated in Fig. 2(b), with the field point \mathbf{P} (at coordinate \mathbf{r}) and the line vector ξ staying on the same plane and \mathbf{n} being this plane's normal vector. The term $(pq)_{jk}$, with vectors \mathbf{p} and \mathbf{q} , is the Christoffel stiffness tensor given by $p_i C_{ijkl} q_j$, and $(pq)_{jk}^{-1}$ is its inverse. The tensors \mathbf{Q} and \mathbf{S}^T are as determined by Asaro and Barnett (1974).

To model collinear dislocation segments, the expression becomes (see Fig. 2(c)) (Yin et al., 2010):

$$\sigma_{kl}(\mathbf{r}) = \left(\frac{1}{|\mathbf{BP}|} - \frac{1}{|\mathbf{AP}|} \right) g_{kl}(\xi) \quad (4)$$

where

$$g_{kl}(\xi) = \frac{1}{8\pi^2} C_{klip} \epsilon_{pjw} b_m C_{wmrs} \xi_j \int_0^{2\pi} \left\{ \xi_s (z' z')_{ir}^{-1} - z'_s [(z' z')^{-1} [(\xi z') + (z' \xi)] (z' z')^{-1}]_{ir} \right\} d\psi \quad (5)$$

The resulting force \mathbf{f} on the original dislocation line segment can be calculated from the stress $\boldsymbol{\sigma}$ using the Peach-Köhler equation $\mathbf{f} = \mathbf{b} \cdot \boldsymbol{\sigma} \times \boldsymbol{\xi}$.

2.3.2. Self-forces

The self-force of a dislocation is the force exerted on a dislocation by itself, which tends to minimise the length of the dislocation and which contains two contributions, the elastic and the core self-force. The elastic self-force is calculated using the same formula as for the collinear dislocation segments (Eqn. 4), but using an inner cutoff radius (Yin et al., 2010) (see Fig. 2(d)). The inner cut-off radius is applied to avoid the singularity arising from classical continuum dislocation theory (Cai et al., 2006) which would lead to a divergence of stress fields computed when the field point is close to the dislocation core. It is usually chosen to be the dislocation core radius. This assumption appears to be reasonable for III-nitrides, as previous critical thickness calculations by Holec et al. (2008) show a good match with experimental data using the core radius as the inner cutoff radius.

The self-force from the core region can be divided into two components: a longitudinal self-force and a torsional self-force (Fitzgerald and Aubry, 2010). The former force will act to reduce the dislocation segment length (thereby minimising its total energy), while the latter force will tend to rotate the segment line direction to a more energetically favourable direction. In an anisotropic elastic space, the core longitudinal force for each dislocation segment is (Fitzgerald and Aubry, 2010):

$$\mathbf{f}_c^L = -\frac{4\pi E_{\text{core}}}{\bar{\mu}|\mathbf{b}|^2}(\mathbf{b} \cdot \mathbf{B} \cdot \mathbf{b})\boldsymbol{\xi} \quad (6)$$

where $\bar{\mu}$ is the anisotropic shear modulus; E_{core} is the core energy; and \mathbf{B} can be calculated by

$$B_{ij} = \frac{1}{8\pi^2} \int_0^{2\pi} \{ (mm)_{ij} - (mn)_{ik}(nn)_{kl}^{-1}(nm)_{lj} \} d\psi \quad (7)$$

And the core torsional force, which tends to rotate the dislocation segments to lower energy configuration, would be (Fitzgerald and Aubry, 2010)

$$\mathbf{f}_c^T = -\frac{4\pi E_{\text{core}}}{\bar{\mu}|\mathbf{b}|^2} \left[\left(\mathbf{b} \cdot \frac{\partial \mathbf{B}}{\partial \phi} \cdot \mathbf{b} \right) \mathbf{e}_\phi + \left(\mathbf{b} \cdot \frac{\partial \mathbf{B}}{\partial \theta} \cdot \mathbf{b} \right) \mathbf{e}_\theta \right] \quad (8)$$

where \mathbf{e}_ϕ and \mathbf{e}_θ are the base vectors as in a spherical coordinate system.

2.3.3. Image forces

The Willis-Steeds-Lothe formula describes the stress fields of dislocations in an infinite anisotropic elastic space, but surfaces and interfaces play a significant role in semiconductor thin films by imposing 'image forces' on the dislocations (Hirth and Lothe, 1982). Expressions already exist for the stress field of a semi-infinite straight dislocation with arbitrary Burgers vector and angle of incidence, terminating at the free surface of an elastically anisotropic semi-infinite solid (Head, 1953b,a; Yoffe, 1961; Lothe et al., 1982). However, to calculate image forces for an arbitrary dislocation microstructure with multiple interfaces, we follow the superposition approach (Fivel et al., 1998; Van der Giessen and Needleman, 1995; Yasin et al., 2001), in which the calculation is decomposed into two separate elastic problems: (1) the problem of interacting dislocations in a homogeneous infinite elastic solid, and (2) a dislocation-free version of the original problem. To account for dislocation-boundary (surface) intersection, the dislocation segment that terminates on the surface is extended up to 1000 times the original segment, producing the 'augmented dislocation configuration' (Deng et al., 2008; Weinberger et al., 2009).

We have therefore used a hybrid finite element method combining the method of superposition of multiple subdomains of Zbib and Díaz de la Rubia (2002) with the virtual segment approach of Weinberger et al. (2009). This provides the flexibility to simulate arbitrary interfaces and surfaces and also has an acceptable accuracy provided that the finite element 'mesh' is fine enough near the dislocation-surface interception point.

To implement this approach, each anisotropic elastic layer is treated separately to satisfy a traction-matching condition at the interfaces. The traction force resulting from the image stress \tilde{T}_i at the interface between the i^{th} and $(i+1)^{\text{th}}$ layer is estimated according to:

$$\tilde{T}_i = \bar{\gamma} T_i^\infty \quad (9)$$

$\mathbf{T} = \boldsymbol{\sigma} \cdot \mathbf{n}$; T_i^∞ is the traction force on the interface in an infinite anisotropic elastic space such that the resulting traction force $\mathbf{T}_i = \mathbf{T}_i^\infty + \tilde{\mathbf{T}}_i$; and $\bar{\gamma} = \frac{\bar{\mu}_{i+1} - \bar{\mu}_i}{\bar{\mu}_{i+1} + \bar{\mu}_i}$. The resulting traction force at the surface with normal \mathbf{n} would be reduced to zero for a traction-free condition with $\bar{\gamma} = -1$, that is, the image traction force would be a 'reverse' of that in the infinite anisotropic elastic space. It is also obvious that there would be no imaging traction force when layer i and layer $i+1$ are the same, causing $\bar{\gamma} = 0$.

Setting \tilde{T}_i as the boundary condition of the finite element calculation, the image stress tensor field can be solved using an external 3D finite element mesh generator *gmsh* (Geuzaine and Remacle, 2009) and solver *getdp* (Dular et al., 1998). Since the

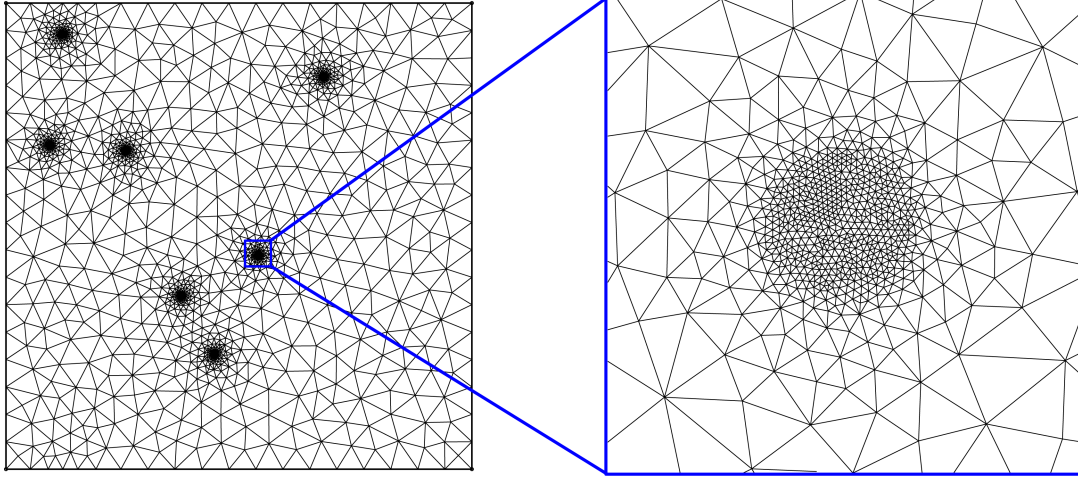


Figure 3: Adaptive mesh on a film surface, showing elements near the dislocation segment which have a dimension of about 2 Å (i.e. atomic scale). The larger area shown has dimensions of 800 nm \times 800 nm.

image force is most intense near surface and interfaces, the mesh is generated such that it is adaptively meshed finely where the dislocation segments intercept with the interfaces and surfaces (Fig. 3). The image stress, when summed with the stress field in infinite anisotropic elastic space as calculated using the Willis-Steeds-Lothe equation, can satisfy both the traction-matching condition at the interfaces and the traction-free condition at the surface. The Willis-Steeds-Lothe equation (originally formulated for an infinite anisotropic space) is thus adapted to compute the stress field of a dislocation in a finite anisotropic space.

2.3.4. Misfit forces

The misfit force arises from the elastic stress generated by the lattice mismatch between film and substrate. To take into account the effect of the stress tensor field from other factors on the misfit force, the lattice parameters on each layer are recalculated every time step from the total stress field excluding the misfit force itself. In this case, the misfit strain $\epsilon_m(t, T)$ on any layer would be

$$\epsilon_m(t, T) = \frac{a'_f(t, T) - a_f(T)}{a_f(T)} \quad (10)$$

where $a'_f(t, T)$ is the recalculated lattice parameter at time t and temperature T ; and $a_f(T)$ is the thermally expanded lattice parameters for the film. Note that Equation 10 follows the convention that compressive strain is negative, and vice

versa. The thermal expansion coefficients $\alpha(T)$ are determined using the Reeber model for GaN and AlN (Reeber and Wang, 2000) and the Suzuki model for InN (Wang and Reeber, 2001), respectively.

Assuming the lattice parameter of the film is lattice-matched to the substrate at time $t = 0$, i.e., $a'_f(0, T) = a_s(T)$, then at this time this equation reduces to the conventionally defined $\epsilon_m = \frac{a_s - a_f}{a_f}$ (Freund and Suresh, 2003), and the re-calculated lattice parameter at any time t is as follows, where ϵ_{\parallel} is the equivalent strain (as calculated from other driving forces) parallel to the direction of a calculated from the strain-displacement equation:

$$a'_f(t, T) = (1 + \epsilon_{\parallel})a_s(T) \quad (11)$$

If the film does not have the same crystallographic orientation as the substrate, then the lattice parameters in Eqn. 10 and Eqn. 11 can be replaced by the atomic plane spacing so that the lattice parameters and can be solved in a system of parametric equations. So in this case, $d'_{f1}(0, T) = d_{s1}(T)$, $d'_{f2}(0, T) = d_{s2}(T)$, then the following applies, where $d_{f1}(t, T) = d_{h_1 k_1 l_1}$ and $d_{f2}(t, T) = d_{h_2 k_2 l_2}$:

$$a_f^2 = \frac{4}{3} \frac{d_{s1}^2 d_{s2}^2 [l_2^2 (h_1^2 + h_1 k_1 + k_1^2) - l_1^2 (h_2^2 + h_2 k_2 + k_2^2)]}{d_{s2}^2 l_2^2 - d_{s1}^2 l_1^2} \quad (12)$$

$$c_f^2 = \frac{d_{s1}^2 d_{s2}^2 [l_2^2 (h_1^2 + h_1 k_1 + k_1^2) - l_1^2 (h_2^2 + h_2 k_2 + k_2^2)]}{d_{s1}^2 (h_1^2 + h_1 k_1 + k_1^2) - d_{s2}^2 (h_2^2 + h_2 k_2 + k_2^2)} \quad (13)$$

The misfit stress on a layer can thus be computed by applying a fixed displacement calculated from the corresponding misfit strain on its side wall in a finite element calculation.

2.3.5. Thermal forces

External biaxial stress mainly originates from the different thermal expansion coefficients and growth temperatures of different layers. The thermal expansion coefficients of materials were included in the misfit force as described in the previous section. However, thermal mismatch stress can be incurred by the difference in thermal expansions and growth temperatures, in addition to the thermal mismatch arising from the lattice parameters due to difference in thermal expansion coefficient. The thermal mismatch force in this section simulates thermal effect from layers grown below the simulation environment. Using the thermal expansion function from Reeber and Wang (2000) and Wang and Reeber (2001), the thermal expansion vector, representing the thermal expansion in 3D, for a \mathbf{c} -plane layer, would be

$$\boldsymbol{\alpha}(T, T_g) = [\alpha_a(T, T_g), \alpha_a(T, T_g), \alpha_c(T, T_g)] \quad (14)$$

where T_g is the growth temperature of the layer, T is the growth temperature during the current time step.

So for a layer with an arbitrary orientation, by rotating the base vectors \mathbf{x} , \mathbf{y} and \mathbf{z} to \mathbf{c} -plane from that orientation, the corresponding in-plane thermal expansion vector would be:

$$\boldsymbol{\alpha}_i(T, T_g) = \boldsymbol{\alpha}(T, T_g) [\mathbf{x}_c^T, \mathbf{y}_c^T, 0] \quad (15)$$

where \mathbf{x}_c and \mathbf{y}_c are the rotated base vectors. Here we assume that the thermal mismatch is a biaxial stress (acting only in planar direction), thus the expansion vector in the vertical (\mathbf{z} -) direction is zeroed. The differential thermal expansion vector can then be calculated from:

$$\Delta\boldsymbol{\alpha}_i(T, T_{g,i}) = \boldsymbol{\alpha}_i(T, T_{g,i}) - \boldsymbol{\alpha}_{(i-1)}(T, T_{g,(i-1)}) \quad (16)$$

with $\Delta\alpha_0 = 0$. Unlike the misfit force, the effect of the thermal force, which would only be dependent on the in-plane thermal mismatch, should be cumulative starting from the substrate, since each layer is grown on top of a thermally expanded previous layer. So the resultant thermal strain on the whole structure, assuming no bending, would be

$$[\epsilon_T(t, T)]_j = \sum_{i=0}^{n(t)} \Delta\alpha_{ij}(T, T_{g,i}) \quad (17)$$

where $n(t)$ is the total number of layers at time t .

The thermal stress and thermal force can then be computed by using a finite element method similar to that for the mismatch stress, but with the fixed displacement calculated from the thermal strain instead.

2.3.6. Osmotic forces

Osmotic forces affect dislocation climb and are generated when a non-equilibrium concentration of point defects arises in the material. This creates a driving force for dislocations to restore equilibrium by the absorption or emission of point defects from the dislocation core (resulting in dislocation climb). The magnitude of the osmotic force is therefore controlled by point defect diffusion, and only contributes to dislocation climb. The point defect concentration field c_v are initialised by assuming that they are initially in equilibrium with dislocations. It is then subjected to bulk diffusion as the dislocations move during the simulation (Hirth and Lothe, 1982):

$$\frac{\partial c_v}{\partial t} = D\Delta c_v \quad (18)$$

where D is the diffusivity. The diffusion of the vacancy concentration is implemented with a finite difference method (FDM) using a 3D forward time, centered space (FTCS) scheme with adaptive time stepping. Section 2.4.2 then describes how the bulk vacancy concentration field is used to approximate climb assisted by pipe diffusion, as according to Turunen and Lindroos (1974) and Turunen (1976).

The effect of dislocation climb by both bulk and pipe diffusion on the vacancy concentration field is approximated by absorption (or emission) of point defects in proportion to the length and the distance travelled by a segment of a dislocation. Thus after each iteration of dislocation motion, the vacancy concentration is modified according to the area (in terms of lattice parameters) swept by each climbing dislocation segment. And the osmotic force f_o would be (Hirth and Lothe, 1982)

$$\frac{f_o}{L} = -\frac{k_B T b_e}{v_a} \ln \frac{c_v}{c_0} \quad (19)$$

where k_B is the Boltzmann's constant; b_e is the edge component of Burgers vector; v_a is the atomic volume; and c_0 is the equilibrium concentration of vacancies, given by (Lothe, 1960; Hirth and Lothe, 1982)

$$c_0(\mathbf{r}) = n_v e^{-\frac{E_f - \sigma(\mathbf{r})\Delta V}{k_B T}} \quad (20)$$

where n_v is the concentration of possible vacancy site; $\sigma(\mathbf{r})$ is the stress experienced by the material at \mathbf{r} causing a change in volume ΔV ; and E_f is the vacancy formation energy.

2.3.7. Peierls forces

The Peierls stress affects dislocation glide, acting as an energy barrier due to the varying misfit energy of the dislocation when it glides along a specific slip plane. This lattice frictional force varies with a periodicity closely related to nearest-neighbour interatomic distances within the material and depends on the slip system in which the dislocation lies. The temperature-dependent Peierls force f_p per unit length L , which includes the effect of thermal fluctuation at finite temperature, can be calculated by Chidambarrao et al. (1990) and Srinivasan et al. (2003):

$$\frac{f_p}{L} = 2\bar{\mu}|\mathbf{b}| \cos \phi \left(\frac{1 - \nu \cos^2 \alpha}{1 - \nu} \omega e^{\left(\frac{-2\pi d_{hkl}(1-\nu \cos^2 \alpha)\omega}{(1-\nu)|\mathbf{b}|} \right)} \right) \quad (21)$$

where ϕ is the angle between the film surface and the normal to the slip plane; α is the angle between the dislocation segment and Burgers vector; ν is the Poisson's

ratio; d_{hkl} is the interplanar spacing of the slip plane (hkl) and ω is given by

$$\omega = e^{-\frac{4\pi^2 n k_B T}{5\bar{\mu} V}} \quad (22)$$

where n is the number of atoms per unit cell; and V is the volume of the unit cell.

2.4. Dislocation mobility

In the model, forces acting on dislocations produce dislocation movement via dislocation mobility functions. These functions convert calculated stresses into realistic simulated glide and climb velocities.

2.4.1. Glide

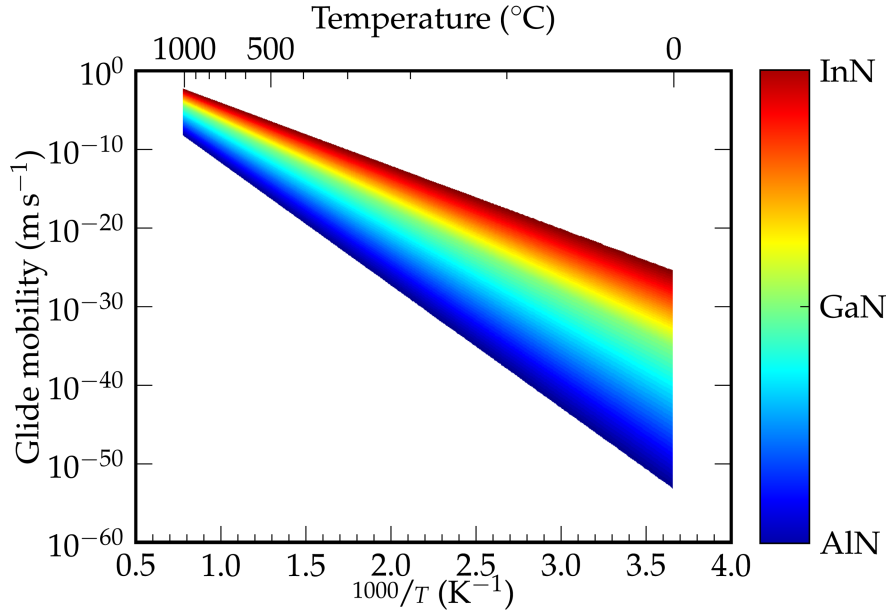


Figure 4: Glide mobility versus temperature plot, calculated from the experimental data of Yonenaga (2003), Yonenaga et al. (2003, 2009) and Sugiura (1997).

The simplest dislocation mobility function was proposed by Hirth and Lothe (1982) who used an arbitrary viscous drag coefficient B to relate the force f_g per unit length L and dislocation glide velocity v_g . Mobility function M (the inverse of B) has been used in some dislocation dynamics simulations in metals, but a suitable value of M has not been proposed for nitrides (Cai and Bulatov, 2004). Although an accurate expression exists for v_g based on the classical theory of kink mobility (Raabe,

1998), several of its variables are unknown. Consequently, recent work has focused on determining B accurately for each material of interest by fitting experimental data or molecular dynamics simulation, resulting in an empirical expression (Fertig and Baker, 2009; Sugiura, 1997). We adapt the expression in this work as:

$$v_g = \left[v_0 \left(\frac{\tau_g}{\tau_0} \right)^m e^{-\frac{Q_g}{k_B T}} \right] (\mathbf{n}_g \times \boldsymbol{\xi}) \quad (23)$$

where v_g is the glide velocity of a dislocation segment; v_0 is a constant; \mathbf{s} is the slip plane normal; τ_g is the resolved shear stress acting on the dislocation segment; τ_0 is a constant (1 MPa); and Q_g is the glide activation energy. From experimental data, for GaN was estimated to be 2.0 eV (Sugiura, 1997) or between 2.0 – 2.7 eV (Yonenaga, 2003; Yonenaga et al., 2003, 2009); whereas from molecular dynamics simulations, for GaN was estimated to be 1.6 eV, 1.6 eV and 4.7 eV for the basal, prismatic and pyramidal planes, respectively (Weingarten and Chung, 2013). The estimated glide mobility of III-nitrides is illustrated in Fig. 4.

To account for dislocation glide in the model, the Peach-Köhler force acting on each dislocation segment is resolved in all the possible slip systems described by Srinivasan et al. (2003). The resolved forces are then compared to the temperature-dependent Peierls forces of the corresponding slip systems. A slip system is designated as active if the net force on it is positive. The final slip direction is then selected according to the largest net glide force.

2.4.2. *Climb*

It is more complicated to determine an accurate mobility function for dislocation climb. Climb can be driven by both hydrostatic and biaxial stresses and by osmotic effects. Climb is typically limited by the mobility of dislocation jogs (Lothe, 1960) and can be enabled by bulk diffusion (i.e. diffusion of vacancies or interstitials through the bulk, towards or away from the dislocation) and/or by pipe diffusion (i.e. the preferential diffusion of vacancies or interstitials along the dislocation core). Pipe diffusion is likely to be highly relevant to III-nitride materials, because strong evidence of dislocation climb exists for GaN (Moram et al., 2010) and AlN (Fu et al., 2011) but both materials have very low vacancy and interstitial self-diffusion coefficients (Laaksonen et al., 2009; Terentjevs et al., 2010) which are expected to lead to very low bulk climb velocities. Consequently, although a simple mobility function has been used to model the climb velocity v_c (Cai and Bulatov, 2004), it cannot capture the complexity of climb processes occurring in real materials. Furthermore, although an expression has been derived for v_c based on the classical theory for bulk climb (Raabe, 1998), several of its variables are unknown and it cannot account for

pipe-diffusion-controlled climb. A simpler expression for bulk climb has also been derived (Clouet, 2011), but it is not applicable to pipe-diffusion-controlled climb either. While climb mobility functions were also derived for both bulk and pipe diffusion of a single jog (Lothe, 1960), these assume that climb is driven only by osmotic forces and do not include any contribution from biaxial stress.

In contrast, Turunen has derived a general equation of motion for a climbing, arbitrarily curved dislocation, taking into account both bulk diffusion (Turunen, 1976) and pipe diffusion (Turunen and Lindroos, 1974; Turunen, 1976) along the dislocation core. The climb velocity is described by:

$$v_c = \left\{ \left(\frac{2\pi V^2 D c_0}{k_B T b_e^2 \ln R/\rho} \right) f_c - \left(\frac{2\nu_0 D \kappa a V^2}{k_B T b_e^2} e^{-\frac{Q_p}{k_B T}} \right) \left[\frac{b_s}{b_e^2} \left(\mathbf{b} \cdot \frac{d\mathbf{u}}{ds} \frac{df_c}{ds} + \frac{d^2 f_c}{ds^2} \right) \right] \right\} \frac{\mathbf{b} \times \boldsymbol{\xi}}{|\mathbf{b} \times \boldsymbol{\xi}|} \quad (24)$$

V is the vacancy volume; f_c is the dislocation climb force; ν_0 is the attempt frequency of atomic jumps; Q_p is the activation energy of pipe diffusion; b_s is the screw component of the Burgers vector; κ is a numerical constant (~ 0.5); a is the jump distance in the dislocation core; R is an outer cutoff radius at $c(\mathbf{r}) = c_0(\mathbf{r})$; ρ represents the dislocation core radius; and \mathbf{s} is a point along the dislocation line. The first term of the equation accounts for climb due to bulk diffusion, while the latter term accounts for climb due to pipe diffusion. The dislocation core is considered as a tunnel along the line direction made up of atomic sites where diffusive jumps could happen. From the climb force f_c and the activation energy required for a diffusion jump Q_p , the effective number of diffused atoms causing climb of the dislocation segment can be related to the climb force, and thus v_c can be calculated from the net atomic flux diffusing along the dislocation core. This expression models both bulk and pipe diffusion and contains parameters that can be either measured or computed for III-nitrides, so therefore it is chosen for use in the simulations.

We note that the $\frac{df_c}{ds}$ in the second term only exists when the dislocation line is not straight, i.e., $\frac{d\mathbf{u}}{ds} \neq 0$: this was omitted in the original work based on the assumption that the dislocation has a low curvature (Turunen, 1976), which breaks down based on the simulations. Another point to note is that the Debye frequency, which is the theoretical maximum of the jump frequency, is more readily available from previous studies and is used as a sensible guess of the actual attempt frequency. It is calculated from the Debye temperature given in Table 2 by $\omega_0 = \frac{k_B \omega_D}{h}$. The Debye temperatures reported for GaN show a wide scatter between 500 K and 900 K and appropriate values have not yet been determined for all III-nitrides. However, the $\hat{\Gamma}$ values used in the fitting of the Varshni formula are closely associated with

the Debye temperatures (Roder et al., 2005; Teisseyre et al., 1994) and are available for all III-nitrides (Vurgaftman and Meyer, 2003), so they have therefore been used in this work.

2.5. Modelling of thin film growth

Typically for nitride semiconductors, the most significant change in dislocation microstructures takes place during the growth of thin films and multilayers. Therefore, a simple growth model is introduced to the dislocation dynamics model, in which the film thickness can increase (or decrease, e.g. during etching) according to a predefined growth rate on each facet on the surface of the film, after which the stress field on dislocations is recalculated at each time step. This approach enables the response of dislocations to the change in film thickness to be modelled.

Complex film structures can then be 'grown' during the simulation using multiple 'growth' steps with step-specific time durations, the growth rate of the individual facet and material types. A simple growth mechanism is implemented such that the dislocation will choose to elongate along the direction of the substrate normal (usually $[0001]$) the surface facet that it is closest to, along other common dislocation directions for nitride films, $\langle 11\bar{2}0 \rangle$ and $\langle 10\bar{1}0 \rangle$, or along the original dislocation line direction, according to the lowest calculated strain energy that will be incurred.

2.6. Choice of parameters used in the model

Table 2 summarises the key material parameters used in the model, with references.

2.6.1. Core radii and core energies

The three types of pure dislocations in III-nitrides are summarised in Table 2. However, approximately 99% of the dislocations found in heteroepitaxial III-nitride structures on sapphire are either \mathbf{a} -type or $(\mathbf{a} + \mathbf{c})$ -type (Moram et al., 2009), apart from at the early stages of film growth where different ratios of different dislocation types can occur. Different core structures are possible (Lymperakis et al., 2004), but the commonest are the 5/7-atom ring structure for \mathbf{a} -type dislocations and the 5/6-atom ring structure for the $(\mathbf{a} + \mathbf{c})$ -type dislocations (Rhode et al., 2013). Therefore, we have used reliable literature values for the core radii and the core energies of dislocations in III-nitrides with these core structures, as listed in Table 3.

2.6.2. Activation energies for dislocation climb

Even though the precise mechanism of climb is not known in the III-nitrides, the activation energy of the rate-limiting step of the climb process can still be identified

Material parameters	Value(s) chosen		References
Elasticity tensor \mathbf{C}	$C_{11,\text{AlN}} = 396$ GPa	$C_{12,\text{AlN}} = 137$ GPa	Wright (1997)
	$C_{13,\text{AlN}} = 108$ GPa	$C_{33,\text{AlN}} = 373$ GPa	
	$C_{44,\text{AlN}} = 116$ GPa		
	$C_{11,\text{GaN}} = 367$ GPa	$C_{12,\text{GaN}} = 135$ GPa	
	$C_{13,\text{GaN}} = 103$ GPa	$C_{33,\text{GaN}} = 405$ GPa	
	$C_{44,\text{GaN}} = 95$ GPa		
Lattice parameters a and c	$C_{11,\text{InN}} = 223$ GPa	$C_{12,\text{InN}} = 115$ GPa	Moram and Vickers (2009)
	$C_{13,\text{InN}} = 92$ GPa	$C_{33,\text{InN}} = 224$ GPa	
	$C_{44,\text{InN}} = 48$ GPa		
Debye temperature θ_D	$a_{\text{AlN}} = 3.111$ Å	$c_{\text{AlN}} = 4.980$ Å	Roder et al. (2005); Teisseyre et al. (1994); Vurgaftman and Meyer (2003)
	$a_{\text{GaN}} = 3.189$ Å	$c_{\text{GaN}} = 5.186$ Å	
	$a_{\text{InN}} = 3.538$ Å	$c_{\text{InN}} = 5.706$ Å	
Dislocation core energy E_{core}	See Table 3		
Temperature dependent thermal expansion function in the \mathbf{a} and \mathbf{c} directions	$a(\text{AlN})$ $a(\text{GaN})$ $a(\text{InN})$	$c(\text{AlN})$ $c(\text{GaN})$ $c(\text{InN})$	Moram and Vickers (2009); Reeber and Wang (2000)
Diffusion coefficients* for bulk diffusion D_B	AlN = $72.1e^{-\frac{4.7}{k_B T}}$ GaN = $43.0e^{-\frac{4.24}{k_B T}}$ InN = $39.8e^{-\frac{2.1}{k_B T}}$		Extrapolated from Ambacher et al. (1998)
Glide activation energy Q_g	$Q_g(\text{AlN}) = 3.1$ eV $Q_g(\text{GaN}) = 2.1$ eV $Q_g(\text{InN}) = 1.2$ eV		Estimated from Sugiura (1997); Yonenaga et al. (2009)
Climb activation energy, for pipe diffusion Q_p	$Q_p(\text{AlN}) = 3.4$ eV $Q_p(\text{GaN}) = 3.7$ eV		Fu et al. (2011); Moram et al. (2010)
Atomic volume V_A	$V_{\text{Al}} = 10.44$ Å ³ $V_{\text{Ga}} = 11.42$ Å ³ $V_{\text{In}} = 15.46$ Å ³		Estimated from lattice parameters Moram and Vickers (2009)

*includes the vacancy or interstitial formation energy, the diffusion coefficient pre-exponential factor and the self-diffusion enthalpy

Table 2: Parameters used in simulations of thin films and multilayers of AlN, GaN, InN and their alloys. N.B. The value for Q_p of InN is currently unknown as the relevant experimental studies are not available in the literature.

by comparison to experimental data. The model was used to simulate the growth of GaN- and AlN-on-sapphire films according to the conditions reported by Moram et al. (2010) and Fu et al. (2011) respectively and average dislocation velocities were obtained. These results were then compared to the average dislocation velocities obtained from the experimental results reported by Moram et al. (2010) and Fu et al. (2011) respectively. The upper and lower error bounds are obtained by assuming no and maximum dislocation inclination responsible for the displacement of dislocation. Fig. 5 shows the average dislocation velocities obtained from simulations and plotted

Material	Burgers vector \mathbf{b}	Core radius ρ (Å)	E_{core} (eV)	Method	Reference
GaN	$(\mathbf{a} + \mathbf{c})$ -type	7.2	3.12	MSW potential	Belabbas et al. (2007)
	\mathbf{a} -type	7.0	1.57	Multiscale DFT with SW potential	Lymperakis (2005)
		6.0	1.61	Many body	Kioseoglou et al. (2009)
AlN	\mathbf{a} -type	8.3	1.71	interatomic Tersoff	
InN		5.4	1.66	potential	

Table 3: Core radii and energies for dislocations in III-nitrides, including \mathbf{a} -type dislocations with 5/7-atom ring cores, and $(\mathbf{a} + \mathbf{c})$ -type dislocations with 5/6-atom ring cores from atomistic simulations.

against different pipe diffusion activation energies for GaN films (each simulation was repeated 10 times; results for AlN were very similar). A small change in Q_p alters the dislocation climb velocities by orders of magnitude, while the simulated climb velocity is much less sensitive to the other simulation parameters. This is as expected considering Eqn. 24 for climb mobility, where the climb velocity is exponentially dependent on the activation energy. From Fig. 5, Q_p for AlN and GaN are thus found to be approximately 3.4 ± 0.45 eV and 3.7 ± 0.40 eV respectively. However, the average climb dislocation velocity estimated from experiment shows that dislocations climb faster in AlN than in GaN, so AlN has a lower pipe diffusion activation energy. The difference in pipe diffusion activation energies between GaN and AlN may be due to relative size effects: the atomic radius of Al is approximately 6% smaller than that of Ga (135 pm and 143 pm, respectively) (Rhode et al., 2013), whereas the lattice parameters and consequently the internal diameters of the dislocation cores are only 2.5% smaller for AlN than for GaN ($a_{\text{AlN}} = 3.111$ Å and $a_{\text{GaN}} = 3.189$ Å) (Moram and Vickers, 2009). In the simulations, the rate of diffusion is proportional to $e^{-\frac{Q_0}{k_B T}}$ and to the cross sectional area of the dislocation pipe πr_c , a decrease in activation energy with increasing relative core radius r_c is expected.

3. Results

The simulations were validated by comparison to transmission electron microscopy data of an AlN epilayer on a sapphire substrate and of an $\text{Al}_{0.87}\text{Ga}_{0.13}\text{N}$ film on an AlN-on-sapphire substrate. For the AlN film on sapphire, the simulation was set up using a simulation cell with a lateral size of $169 \text{ nm} \times 169 \text{ nm}$ containing 10 dislocations with randomly assigned Burgers vector directions and with types as-

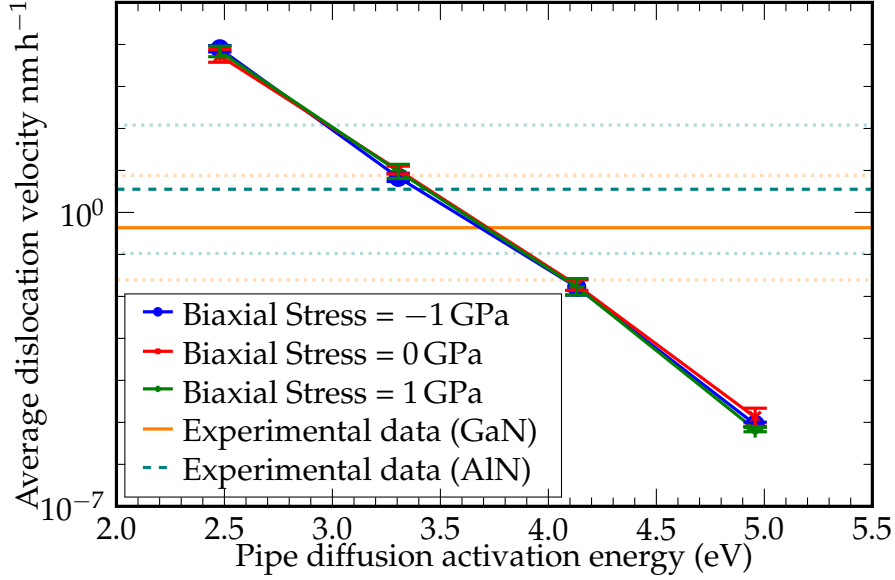


Figure 5: Average dislocation velocities plotted versus pipe diffusion activation energy, subjected to different external biaxial stresses. Experimental data for GaN and AlN are extracted from the results of Moram et al. (2010) (solid orange line) and Fu et al. (2011) (dashed greenish blue line), respectively. Their error ranges are represented by the dotted lines with light orange colour for GaN and light greenish blue colour for AlN.

signed randomly according to the proportions found experimentally. In this case, the simulations included three \mathbf{a} -type dislocations, six \mathbf{c} -type dislocations and one $(\mathbf{a} + \mathbf{c})$ -type dislocation, as these ratios are in proportion to the amounts of different types of dislocations found experimentally at the very early stages of film growth (Fu et al., 2011) (note that the proportion of \mathbf{a} -type dislocations rises greatly as the film thickness increases, because \mathbf{c} -type dislocations tend to annihilate each other easily during the initial stages of film growth (Fu et al., 2011)). All other settings were based on experimental growth parameters, including an epilayer growth temperature of 1403 K and a growth rate of $1.3 \mu\text{m hr}^{-1}$. Here, a free surface was defined at the bottom of the AlN film to simulate the effects of the disordered nucleation layer found experimentally between AlN films and sapphire substrates. The effects of the experimentally verified sapphire substrate miscut of 0.25° towards the $[11\bar{2}0]$ direction were tested by performing one simulation including the miscut and one simulation without it.

For the $\text{Al}_{0.87}\text{Ga}_{0.13}\text{N}$ film on AlN, the simulation was set up using a simulation cell with a lateral size of $396 \text{ nm} \times 396 \text{ nm}$ containing 10 dislocations with randomly

assigned Burgers vector directions and with types assigned randomly according to the proportions found experimentally, in this case nine a-type dislocations and one ($\mathbf{a} + \mathbf{c}$)-type dislocation. All other settings were based on experimental growth parameters, including an epilayer growth temperature of 1382 K and a growth rate of $2 \mu\text{m hr}^{-1}$. The interface is a continuum boundary and the simulations were initiated assuming that the pre-existing dislocations in the AlN layer (beneath the AlGaIn film) were initially straight and aligned along $[0001]$.

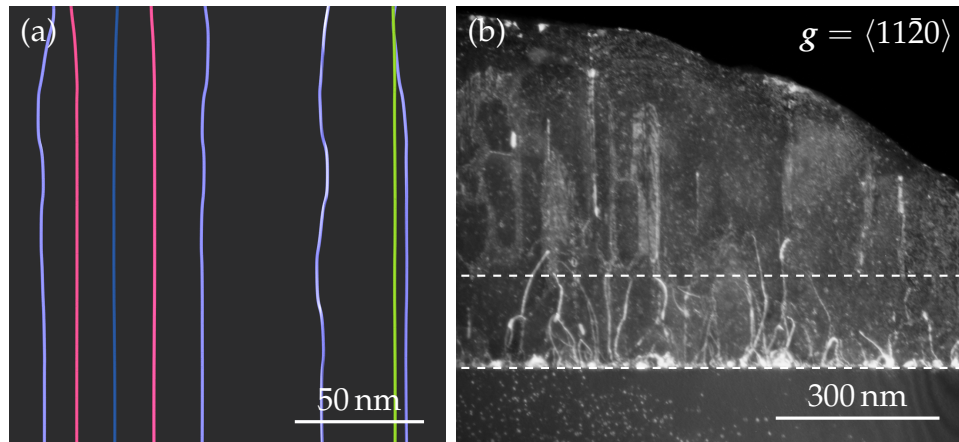


Figure 6: (a) Simulation of an AlN film grown on sapphire with a substrate miscut of 0.25° towards $[11\bar{2}0]$; (b) cross-sectional weak-beam dark field transmission electron micrograph of a $1\text{ }\mu\text{m}$ thick AlN film grown on a sapphire substrate, with a substrate miscut of $0.25 \pm 0.10^\circ$ towards $[11\bar{2}0]$. The micrograph was taken in the $g(5g)$ condition with $g = 11\bar{2}0$, revealing a -type and $(a+c)$ -type dislocations. The plane of the TEM foil and the plane on which the contents of the simulation cell are projected is $(10\bar{1}0)$. Different colours are used for each dislocation in the simulation, for ease of identification. The upper and lower dashed lines in (b) correspond to the vertical boundaries of the simulation as in (a).

Fig. 6 shows the simulation results and the corresponding experimentally determined microstructure for the AlN film on sapphire. The colours of the dislocations in the figure represent their corresponding Burgers vectors (b_x , b_y and b_z are mapped to red, green and blue colours, respectively). No dislocation bending is predicted in simulations of the growth of AlN on sapphire without any miscut: all dislocations remain oriented parallel to $[0001]$. However, when a substrate miscut is included in the simulations, the model reproduces accurately the effects of the miscut on the microstructure of the AlN films. For example, the substrate miscut of 0.25° towards $[11\bar{2}0]$ results in the onset of dislocation bending away from $[0001]$ at an AlN thickness of approximately 150 nm, consistent with experimental data. These data indicate that the substrate miscut has an important role to play in inducing disloca-

tion bending, which is well known to result in an increase in dislocation annihilation and reduction with increasing epilayer thickness in III-nitride films.

Fig. 7 shows the simulation results and the corresponding experimentally determined microstructure for the $\text{Al}_{0.87}\text{Ga}_{0.13}\text{N}/\text{AlN}$ heterostructure. The average (projected) dislocation bending angle away from $[0001]$ in the TEM specimen was $6.7^\circ \pm 1.4^\circ$, whereas the projected dislocation bending angle away from $[0001]$ from the simulations was $6.7^\circ \pm 0.6^\circ$, i.e. the same, within the standard error. Minor differences may relate to the fact that the image force from the $\text{AlN}/\text{sapphire}$ interface was not included in this simulation to minimise computational expense, as the microstructure was expected to be dominated by the effects of misfit stresses at the $\text{Al}_{0.87}\text{Ga}_{0.13}\text{N}/\text{AlN}$ interface. The simulations match the experimental microstructure accurately and are consistent with the low experimentally observed strain relaxation of 6%. These results are in contrast to widely cited equilibrium critical thickness calculations for the $\text{Al}_x\text{Ga}_{1-x}\text{N}/\text{AlN}$ system (equivalent to the inverse of the $\text{Al}_x\text{Ga}_{1-x}\text{N}/\text{GaN}$ calculations), which predict incorrectly that stress relaxation should occur by dislocation glide at an $\text{Al}_{0.87}\text{Ga}_{0.13}\text{N}$ thickness of just 80 nm (Holec et al., 2008). The discrepancy occurs because the equilibrium critical thickness calculations assume that dislocation glide is the only stress relief mechanism that can act in these heterostructures, whereas our model includes the effects of dislocation climb, of image stresses and of the influence of neighbouring dislocations (each with their own strain field). This result indicates that dislocation climb plays an important role in stress relaxation in AlGaN-based heterostructures. The effects of dislocation climb on critical thicknesses for stress relaxation will be explored further in a subsequent publication.

4. Discussions

Table 4 shows a list of 3D discrete dislocation dynamics simulation packages, including this model. A comparison of our model considering the crucial features for simulating dislocation dynamics in thin film nitride semiconductors is also presented. Most of the newer packages have incorporated elastic anisotropy, although only microMegas has explicitly stated and demonstrated the ability to handle hexagonal crystals (Monnet et al., 2004). Most of the packages have been used to study strained epitaxial films with a heterointerface terminated by a free surface, although only MDDP (Zbib and Díaz de la Rubia, 2002) and PDD (Ghoniem and Han, 2005) have demonstrated the ability to handle multilayered structures (i.e. those containing more than two layers). However, most of these studies focus on the ‘channelling stress’, that is, the thickness-dependent critical stress driving a threading dislocation

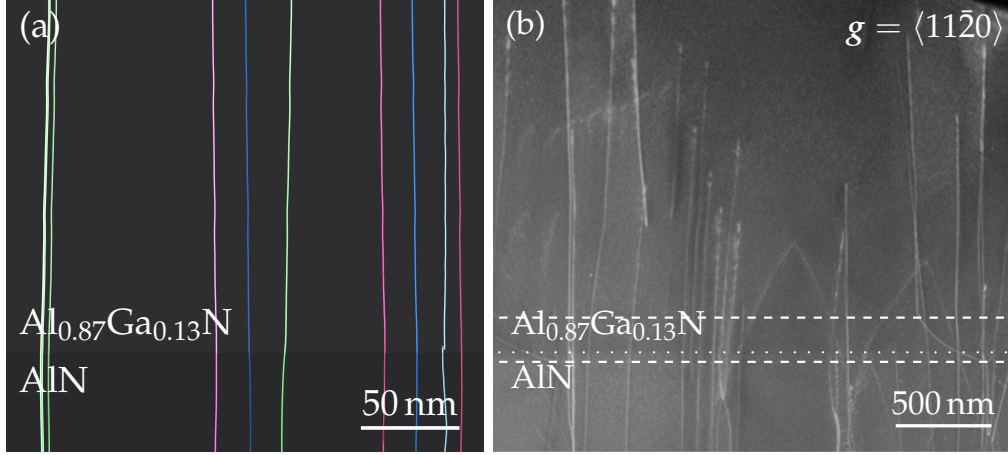


Figure 7: (a) Simulation of an $\text{Al}_{0.87}\text{Ga}_{0.13}\text{N}$ film grown on sapphire with a substrate miscut of 0.25° towards $[11\bar{2}0]$; (b) cross-sectional weak-beam dark field transmission electron micrograph of an $\text{Al}_{0.87}\text{Ga}_{0.13}\text{N}$ film on an AlN buffer layer. The micrograph was taken in the $g(5g)$ condition with $g = 11\bar{2}0$, revealing a -type and $(a + c)$ -type dislocations. The plane of the TEM foil and the plane on which the contents of the simulation cell are projected is $(10\bar{1}0)$. Different colours are used for each dislocation in the simulation, for ease of identification. The upper and lower dashed lines in (b) correspond to the vertical boundaries of the simulation as in (a). The dotted line represents the heterointerface of $\text{Al}_{0.87}\text{Ga}_{0.13}\text{N}/\text{AlN}$.

to introduce a misfit segment. Realistic misfit stresses are much less studied and data appear only for metallic heterointerfaces (Groh et al., 2003), rather than for semiconductors. Therefore, the key advantage of the present approach is the successful implementation and combination of the following features:

- i. The ability to handle both climb and glide, including climb driven by both osmotic and mechanical stresses and enabled by both bulk and pipe diffusion.
- ii. Full elastic anisotropy for materials with hexagonal symmetry.
- iii. Efficient calculations for thin film multilayers and free surfaces, including irregular geometries (e.g. islanded layers), using a superposition method (Tan and Sun, 2006).
- iv. Ability to simulate dislocation dynamics under different thin film growth conditions, including the effects of changes in growth temperature between different layers in a heterostructure.

5. Conclusions

In this work we have described PANIC, a new model for discrete dislocation dynamics simulations which uses an adaptive multi-scale meshing approach combined

Simulation code	Discretization	Stress calculation	Anisotropy	hcp	Free surface	Multi-layer	Misfit forces	Climb	References
This model	Straight line	Willis-Steed-Lothe	Yes	Yes	Yes	Yes	Yes	Yes (bulk and pipe)	-
K-D	Edge-screw	Brown		Yes (line tension)	Yes	Bilayer	Yes		Brown (1964); Groh et al. (2003)
MDDP	Straight line	Simple dislocation bend			Yes	Yes	Yes		Zbib et al. (2001); Zbib and Díaz de la Rubia (2002); Akasheh et al. (2007)
microMega	Straight line	Modified de Wit	Yes	Yes	Yes				Devincere (1995); Monnet et al. (2004); Devincere et al. (2011)
ParaDiS	Straight line	Willis-Steed-Lothe	Yes		Yes			Yes (glide-like mobility law)	Bulatov et al. (2004); Cai and Bulatov (2004); Meijie et al. (2006); Arsenlis et al. (2007); Yin et al. (2010)
PARANOID	Tracking points	Modified Brown			Yes	Bilayer	Yes		Schwarz and Tersoff (1996); Schwarz (1999); Liu and Schwarz (2005)
PDD	Cubic spline	Han and Ghoniem		Yes	Yes	Yes (planar films)	Yes	Yes (bulk)	Ghoniem et al. (2000); Han et al. (2003); Ghoniem and Han (2005)
Tridis	Edge-screw	Modified de Wit			Yes			Yes (bulk)	Devincere (1995); Hartmaier et al. (1999); Mordehai et al. (2008)
VGA	Tracking points	Modified Brown		No	Yes	Bilayer	Yes		Schwarz (1999); von Blanckenhagen et al. (2001, 2004)
W	Straight line	Brown			Yes				Brown (1964); Weygand et al. (2002)

Table 4: A list of 3D discrete dislocation dynamics simulation packages available currently, including features that are either published or explicitly described in the corresponding model's description in the accompanying manual or on the relevant host website.

with input from atomistic simulations to reproduce mesoscale dislocation behaviour. This code can accommodate both hexagonal and cubic materials and includes the full effects of elastic anisotropy. Multilayer structures can be simulated, including the effects of multiple free surfaces and interfaces. Misfit forces and thermal stresses can be included, while arbitrary geometries (both planar and non-planar) can also be simulated. This code has been validated for the case of technologically important AlN and AlGaIn-based thin film heterostructures, for which simulation code inputs are well known. This is the first dislocation dynamics simulation to accurately model dislocation behaviour within semiconductor heterostructures: it is therefore anticipated that the code will facilitate the design and development of devices including defect-containing heterostructures, especially for the challenging III-nitride materials system.

Acknowledgement

WYF acknowledges funding through a Croucher Foundation Scholarship. MAM acknowledges funding through a Royal Society University Research Fellowship and through EPSRC grant no. EP/J015792. This work was performed using the Darwin Supercomputer of the University of Cambridge High Performance Computing Service, provided by Dell Inc. using Strategic Research Infrastructure Funding from the Higher Education Funding Council for England and funding from the Science and Technology Facilities Council.

References

- Akashch, F., Zbib, H. M., Hirth, J. P., Hoagland, R. G., Misra, A., 2007. Dislocation dynamics analysis of dislocation intersections in nanoscale metallic multilayered composites. *Journal of Applied Physics* 101 (8), 084314.
- Amano, H., Iwaya, M., Hayashi, N., Kashima, T., Nitta, S., Wetzel, C., Akasaki, I., 1999. Control of Dislocations and Stress in AlGaIn on Sapphire Using a Low Temperature Interlayer. *physica status solidi (b)* 216 (1), 683–689.
- Ambacher, O., Freudenberger, F., Dimitrov, R., Angerer, H., Stutzmann, M., 1998. Nitrogen Effusion and Self-Diffusion in Ga₁₄N/Ga₁₅N Isotope Heterostructures. *Japanese Journal of Applied Physics* 37, 2416.
- Arsenlis, A., Cai, W., Tang, M., Rhee, M., Oppelstrup, T., Hommes, G., Pierce, T. G., Bulatov, V. V., 2007. Enabling strain hardening simulations with dislocation

- dynamics. *Modelling and Simulation in Materials Science and Engineering* 15 (6), 553.
- Asaro, R. J., Barnett, D. M., 1974. On some three-dimensional dislocation problems in anisotropic media. *Journal of Physics F: Metal Physics* 4 (5), L103.
- Ayas, C., van Dommelen, J., Deshpande, V., 2014. Climb-enabled discrete dislocation plasticity. *Journal of the Mechanics and Physics of Solids* 62, 113–136.
- Belabbas, I., Béré, A., Chen, J., Petit, S., Belkhir, M. A., Ruterana, P., Nouet, G., 2007. Atomistic modeling of the $(a + c)$ -mixed dislocation core in wurtzite GaN. *Physical Review B* 75 (11), 115201.
- Brown, L. M., 1964. The self-stress of dislocations and the shape of extended nodes. *Philosophical Magazine* 10 (105), 441–466.
- Brown, L. M., 1967. A proof of lothe’s theorem. *Philosophical Magazine* 15 (134), 363–370.
- Bulatov, V., Abraham, F. F., Kubin, L., Devincere, B., Yip, S., 1998. Connecting atomistic and mesoscale simulations of crystal plasticity. *Nature* 391 (6668), 669–672.
- Bulatov, V., Cai, W., Fier, J., Hiratani, M., Hommes, G., Pierce, T., Tang, M., Rhee, M., Yates, K., Arsenlis, T., 2004. Scalable Line Dynamics in ParaDiS. SC \check{S} 04. IEEE Computer Society.
- Cai, W., Arsenlis, A., Weinberger, C. R., Bulatov, V. V., 2006. A non-singular continuum theory of dislocations. *Journal of the Mechanics and Physics of Solids* 54 (3), 561–587.
- Cai, W., Bulatov, V. V., 2004. Mobility laws in dislocation dynamics simulations. *Materials Science and Engineering: A* 387-389, 277–281.
- Chan, C.-H., Hou, C.-H., Tseng, S.-Z., Chen, T.-J., Chien, H.-T., Hsiao, F.-L., Lee, C.-C., Tsai, Y.-L., Chen, C.-C., 2009. Improved output power of GaN-based light-emitting diodes grown on a nanopatterned sapphire substrate. *Applied Physics Letters* 95 (1), 011110.
- Chang, T. Y., Moram, M. A., McAleese, C., Kappers, M. J., Humphreys, C. J., 2010. Inclined dislocation arrays in AlGaIn/AlGaIn quantum well structures emitting at 290 nm. *Journal of Applied Physics* 108 (12), 123522.

- Cherns, P. D., McAleese, C., Kappers, M. J., Humphreys, C. J., 2008. Strain Relaxation in an AlGaIn/GaN Quantum Well System. In: Cullis, A. G., Midgley, P. A. (Eds.), *Microscopy of Semiconducting Materials 2007*. Vol. 120 of Springer Proceedings in Physics. Springer Netherlands, pp. 25–28.
- Chidambarrao, D., Srinivasan, G. R., Cunningham, B., Murthy, C. S., 1990. Effects of Peierls barrier and epithreading dislocation orientation on the critical thickness in heteroepitaxial structures. *Applied Physics Letters* 57 (10), 1001.
- Clouet, E., 2011. Predicting dislocation climb: Classical modeling versus atomistic simulations. *Physical Review B* 84 (9), 092106.
- Costa, P. M., Datta, R., Kappers, M. J., Vickers, M. E., Humphreys, C. J., 2005. Misfit dislocations in green-emitting InGaIn/GaN quantum well structures. *MRS Proceedings* 892, FF25–01.
- Cottrell, A. H., 1963. *Dislocations and plastic flow in crystals*. Clarendon Press.
- Cserti, J., Khantha, M., Vitek, V., Pope, D., 1992. An atomistic study of the dislocation core structures and mechanical behavior of a model D0₁₉ alloy. *Materials Science and Engineering: A* 152 (1-2), 95–102.
- Dadgar, A., Bläsing, J., Diez, A., Alam, A., Heuken, M., Krost, A., 2000. Metalorganic Chemical Vapor Phase Epitaxy of Crack-Free GaN on Si (111) Exceeding 1 μ m in Thickness. *Japanese Journal of Applied Physics* 39 (Part 2, No. 11B), L1183–L1185.
- Deng, J., El-Azab, A., Larson, B., 2008. On the elastic boundary value problem of dislocations in bounded crystals. *Philosophical Magazine* 88 (30-32), 3527–3548.
- Devincre, B., 1995. Three dimensional stress field expressions for straight dislocation segments. *Solid State Communications* 93 (11), 875–878.
- Devincre, B., Madec, R., Monnet, G., Queyreau, S., Gatti, R., Kubin, L., 2011. Modeling crystal plasticity with dislocation dynamics simulations: The 'microMegas' code.
- Dular, P., Geuzaine, C., Henrotte, F., Legros, W., 1998. A general environment for the treatment of discrete problems and its application to the finite element method. *Ieee Transactions on Magnetics* 34 (5), 3395–3398.

- Fang, Q. F., Wang, R., 2000. Atomistic simulation of the atomic structure and diffusion within the core region of an edge dislocation in aluminum. *Physical Review B* 62 (14), 9317–9324.
- Fertig, R. S., Baker, S. P., 2009. Simulation of dislocations and strength in thin films: A review. *Progress in Materials Science* 54 (6), 874–908.
- Fitzgerald, S. P., Aubry, S., 2010. Self-force on dislocation segments in anisotropic crystals. *Journal of Physics: Condensed Matter* 22 (29), 295403.
- Fivel, M., Robertson, C., Canova, G., Boulanger, L., 1998. Three-dimensional modeling of indent-induced plastic zone at a mesoscale. *Acta Materialia* 46 (17), 6183–6194.
- Forghani, K., Schade, L., Schwarz, U. T., Lipski, F., Klein, O., Kaiser, U., Scholz, F., 2012. Strain and defects in Si-doped (Al)GaN epitaxial layers. *Journal of Applied Physics* 112 (9), 093102.
- Freund, L. B., Suresh, S., 2003. *Thin Film Materials: Stress, Defect Formation and Surface Evolution*. Cambridge University Press.
- Fu, W. Y., Kappers, M. J., Zhang, Y., Humphreys, C. J., Moram, M. A., 2011. Dislocation Climb in *c*-Plane AlN Films. *Applied Physics Express* 4 (6), 65503.
- Furitsch, M., Avramescu, A., Eichler, C., Engl, K., Leber, A., Miler, A., Rumbolz, C., Brüderl, G., Strauß, U., Lell, A., Härle, V., 2006. Comparison of degradation mechanisms of blue-violet laser diodes grown on SiC and GaN substrates. *physica status solidi (a)* 203 (7), 1797–1801.
- Geuzaine, C., Remacle, J.-F., 2009. Gmsh: A 3-D finite element mesh generator with built-in pre- and post-processing facilities. *International Journal for Numerical Methods in Engineering* 79 (11), 1309–1331.
- Ghoniem, N. M., Han, X., 2005. Dislocation motion in anisotropic multilayer materials. *Philosophical Magazine* 85 (24), 2809–2830.
- Ghoniem, N. M., Tong, S.-H., Sun, L. Z., 2000. Parametric dislocation dynamics: A thermodynamics-based approach to investigations of mesoscopic plastic deformation. *Physical Review B* 61 (2), 913–927.
- Groh, S., Devincre, B., Kubin, L. P., Roos, A., Feyel, F., Chaboche, J.-L., 2003. Dislocations and elastic anisotropy in heteroepitaxial metallic thin films. *Philosophical Magazine Letters* 83 (5), 303–313.

- Haeberlen, M., Zhu, D., McAleese, C., Kappers, M. J., Humphreys, C. J., 2010. Dislocation reduction in MOVPE grown GaN layers on (111)Si using SiN_x and AlGaN layers. *Journal of Physics: Conference Series* 209 (1), 012017.
- Han, J., Waldrip, K. E., Lee, S. R., Figiel, J. J., Hearne, S. J., Petersen, G. A., Myers, S. M., 2001. Control and elimination of cracking of AlGaN using low-temperature AlGaN interlayers. *Applied Physics Letters* 78 (1), 67.
- Han, X., Ghoniem, N. M., Wang, Z., 2003. Parametric dislocation dynamics of anisotropic crystals. *Philosophical Magazine* 83 (31-34), 3705–3721.
- Hartmaier, A., Fivel, M. C., Canova, G. R., Gumbsch, P., 1999. Image stresses in a free-standing thin film. *Modelling and Simulation in Materials Science and Engineering* 7 (5), 781.
- Head, A., 1953a. X. The interaction of dislocations and boundaries. *Philosophical Magazine Series 7* 44 (348), 92–94.
- Head, A. K., 1953b. Edge Dislocations in Inhomogeneous Media. *Proceedings of the Physical Society B* 66 (9), 793.
- Hirsch, P. B., Horne, R. W., Whelan, M. J., 1956. LXVIII. Direct observations of the arrangement and motion of dislocations in aluminium. *Philosophical Magazine* 1 (7), 677–684.
- Hirth, J. P., Lothe, J., 1982. *Theory of dislocations*, 2nd Edition. John-Wiley & Sons.
- Holec, D., Zhang, Y., Rao, D. V. S., Kappers, M. J., McAleese, C., Humphreys, C. J., 2008. Equilibrium critical thickness for misfit dislocations in III-nitrides. *Journal of Applied Physics* 104 (12), 123514.
- Hsu, P. S., Hardy, M. T., Young, E. C., Romanov, A. E., DenBaars, S. P., Nakamura, S., Speck, J. S., 2012. Stress relaxation and critical thickness for misfit dislocation formation in $(10\bar{1}0)$ and $(30\bar{3}1)$ InGa N /Ga N heteroepitaxy. *Applied Physics Letters* 100 (17), 171917.
- Hsu, P. S., Young, E. C., Romanov, A. E., Fujito, K., DenBaars, S. P., Nakamura, S., Speck, J. S., 2011. Misfit dislocation formation via pre-existing threading dislocation glide in $(11\bar{2}2)$ semipolar heteroepitaxy. *Applied Physics Letters* 99 (8), 081912.

- Kaun, S. W., Wong, M. H., Dasgupta, S., Choi, S., Chung, R., Mishra, U. K., Speck, J. S., 2011. Effects of Threading Dislocation Density on the Gate Leakage of AlGaIn/GaN Heterostructures for High Electron Mobility Transistors. *Applied Physics Express* 4 (2), 024101.
- Khan, A., Balakrishnan, K., Katona, T., 2008. Ultraviolet light-emitting diodes based on group three nitrides. *Nature Photonics* 2 (2), 77–84.
- Kioseoglou, J., Komninou, P., Karakostas, T., 2009. Core models of a -edge threading dislocations in wurtzite III(Al,Ga,In)-nitrides. *physica status solidi (a)* 206 (8), 1931–1935.
- Krost, A., Dadgar, A., 2002. GaN-Based Devices on Si. *physica status solidi (a)* 194 (2), 361–375.
- Laaksonen, K., Ganchenkova, M. G., Nieminen, R. M., 2009. Vacancies in wurtzite GaN and AlN. *Journal of Physics: Condensed Matter* 21 (1), 015803.
- Liu, X. H., Schwarz, K. W., 2005. Modelling of dislocations intersecting a free surface. *Modelling and Simulation in Materials Science and Engineering* 13 (8), 1233.
- Lothe, J., 1960. Theory of dislocation climb in metals. *Journal of Applied Physics* 31 (6), 1077–1087.
- Lothe, J., 1967. Dislocation bends in anisotropic media. *Philosophical Magazine* 15 (134), 353–362.
- Lothe, J., Indenbom, V. L., Chamrov, V. A., 1982. Elastic field and self-force of dislocations emerging at the free surfaces of an anisotropic halfspace. *physica status solidi (b)* 111 (2), 671–677.
- Lymperakis, L., 2005. Ab-initio Based Multiscale Calculations of Extended Defects in and on Group III-nitrides. Ph.D. thesis, Universität Paderborn.
- Lymperakis, L., Neugebauer, J., Albrecht, M., Remmele, T., Strunk, H. P., 2004. Strain Induced Deep Electronic States around Threading Dislocations in GaN. *Physical Review Letters* 93 (19), 196401.
- Mathews, J. H., Fink, K. D., 2006. Numerical Methods Using MATLAB. Pearson Education, Limited.

- Matsumoto, M., Nishimura, T., 1998. Mersenne twister: a 623-dimensionally equidistributed uniform pseudo-random number generator. *ACM Trans. Model. Comput. Simul.* 8 (1), 3–30.
- McAleese, C., Kappers, M. J., Rayment, F. D. G., Cherns, P., Humphreys, C. J., 2004. Strain effects of AlN interlayers for MOVPE growth of crack-free AlGaIn and AlN/GaN multilayers on GaN. *Journal of Crystal Growth* 272 (1-4), 475–480.
- Meijie, T., Cai, W., Xu, G., Bulatov, V. V., Tang, M., 2006. A hybrid method for computing forces on curved dislocations intersecting free surfaces in three-dimensional dislocation dynamics. *Modelling and Simulation in Materials Science and Engineering* 14 (7), 1139.
- Monnet, G., Devincre, B., Kubin, L., 2004. Dislocation study of prismatic slip systems and their interactions in hexagonal close packed metals: application to zirconium. *Acta Materialia* 52 (14), 4317–4328.
- Moram, M. A., Ghedia, C. S., Rao, D. V. S., Barnard, J. S., Zhang, Y., Kappers, M. J., Humphreys, C. J., 2009. On the origin of threading dislocations in GaN films. *Journal of Applied Physics* 106 (7), 073513.
- Moram, M. A., Kappers, M. J., Massabuau, F., Oliver, R. A., Humphreys, C. J., 2011a. Response to "Comment on 'The effects of Si doping on dislocation movement and tensile stress in GaN films'" [*J. Appl. Phys.* 109, 073509 (2011)]. *Journal of Applied Physics* 110 (9), 096102.
- Moram, M. A., Kappers, M. J., Massabuau, F., Oliver, R. A., Humphreys, C. J., 2011b. The effects of Si doping on dislocation movement and tensile stress in GaN films. *Journal of Applied Physics* 109 (7), 073509.
- Moram, M. A., Sadler, T. C., Haberen, M., Kappers, M. J., Humphreys, C. J., 2010. Dislocation movement in GaN films. *Applied Physics Letters* 97 (26), 261903–261907.
- Moram, M. A., Vickers, M. E., 2009. X-ray diffraction of III-nitrides. *Reports on Progress in Physics* 72 (3), 36502.
- Mordehai, D., Clouet, E., Fivel, M., Verdier, M., 2008. Introducing dislocation climb by bulk diffusion in discrete dislocation dynamics. *Philosophical Magazine* 88 (6), 899–925.

- Mukai, T., Morita, D., Yamamoto, M., Akaishi, K., Matoba, K., Yasutomo, K., Kasai, Y., Sano, M., Nagahama, S.-i., 2006. Investigation of optical-output-power degradation in 365-nm UV-LEDs. *physica status solidi (c)* 3 (6), 2211–2214.
- Olmsted, D. L., Jr, L. G. H., Curtin, W. A., Clifton, R. J., 2005. Atomistic simulations of dislocation mobility in Al, Ni and Al/Mg alloys. *Modelling and Simulation in Materials Science and Engineering* 13 (3), 371.
- Orowan, E., 1934a. Zur Kristallplastizität. i. *Zeitschrift für Physik* 89 (9-10), 605–613.
- Orowan, E., 1934b. Zur Kristallplastizität. ii. *Zeitschrift für Physik* 89 (9-10), 614–633.
- Orowan, E., 1934c. Zur Kristallplastizität. iii. *Zeitschrift für Physik* 89 (9-10), 634–659.
- Polanyi, M., 1934. Über eine art gitterstörung, die einen kristall plastisch machen könnte. *Zeitschrift für Physik* 89 (9-10), 660–664.
- Raabe, D., 1998. Computational materials science: the simulation of materials microstructures and properties. Wiley-VCH.
- Reeber, R. R., Wang, K., 2000. Lattice parameters and thermal expansion of important semiconductors and their substrates 622, T6.35.
- Rhode, S. K., Horton, M. K., Kappers, M. J., Zhang, S., Humphreys, C. J., Dusane, R. O., Sahonta, S. L., Moram, M. A., 2013. Mg Doping Affects Dislocation Core Structures in GaN. *Physical Review Letters* 111 (2), 025502.
- Roder, C., Einfeldt, S., Figge, S., Hommel, D., 2005. Temperature dependence of the thermal expansion of GaN. *Physical Review B* 72 (8), 085218.
- Schwarz, K. W., 1999. Simulation of dislocations on the mesoscopic scale. I. Methods and examples. *Journal of Applied Physics* 85 (1), 108–119.
- Schwarz, K. W., Tersoff, J., 1996. Interaction of threading and misfit dislocations in a strained epitaxial layer. *Applied Physics Letters* 69 (9), 1220–1222.
- Srinivasan, S., Geng, L., Liu, R., Ponce, F. A., Narukawa, Y., Tanaka, S., 2003. Slip systems and misfit dislocations in InGaN epilayers. *Applied Physics Letters* 83 (25), 5187–5189.

- Steeds, J. W., 1973. Introduction to anisotropic elasticity theory of dislocations. Clarendon Press.
- Sugiura, L., 1997. Dislocation motion in GaN light-emitting devices and its effect on device lifetime. *Journal of Applied Physics* 81 (4), 1633–1638.
- Tan, E. H., Sun, L. Z., 2006. Stress field due to a dislocation loop in a heterogeneous thin film-substrate system. *Modelling and Simulation in Materials Science and Engineering* 14 (6), 993.
- Tapajna, M., Kaun, S. W., Wong, M. H., Gao, F., Palacios, T., Mishra, U. K., Speck, J. S., Kuball, M., 2011. Influence of threading dislocation density on early degradation in AlGaIn/GaN high electron mobility transistors. *Applied Physics Letters* 99 (22), 223501.
- Taylor, G. I., 1934. The Mechanism of Plastic Deformation of Crystals. Part I. Theoretical. *Proceedings of the Royal Society of London A* 145 (855), 362–387.
- Teisseyre, H., Perlin, P., Suski, T., Grzegory, I., Porowski, S., Jun, J., Pietraszko, A., Moustakas, T. D., 1994. Temperature dependence of the energy gap in GaN bulk single crystals and epitaxial layer. *Journal of Applied Physics* 76 (4), 2429.
- Terentjevs, A., Catellani, A., Cicero, G., 2010. Nitrogen vacancies at InN (1100) surfaces: A theoretical study. *Applied Physics Letters* 96 (17), 171901.
- Turunen, M. J., 1976. A general equation of motion for dislocation climb. *Acta Metallurgica* 24 (5), 463–467.
- Turunen, M. J., Lindroos, V. K., 1974. Model for dislocation climb by a pipe diffusion mechanism. *Philosophical Magazine* 29 (4), 701–708.
- Van der Giessen, E., Needleman, A., 1995. Discrete dislocation plasticity: a simple planar model. *Modelling and Simulation in Materials Science and Engineering* 3 (5), 689.
- von Blanckenhagen, B., Arzt, E., Gumbsch, P., 2004. Discrete dislocation simulation of plastic deformation in metal thin films. *Acta Materialia* 52 (3), 773–784.
- von Blanckenhagen, B., Gumbsch, P., Arzt, E., 2001. Dislocation sources in discrete dislocation simulations of thin-film plasticity and the Hall-Petch relation. *Modelling and Simulation in Materials Science and Engineering* 9 (3), 157.

- Vurgaftman, I., Meyer, J. R., 2003. Band parameters for nitrogen-containing semiconductors. *Journal of Applied Physics* 94 (6), 3675–3696.
- Wang, K., Reeber, R. R., 2001. Thermal expansion and elastic properties of InN. *Applied Physics Letters* 79 (11), 1602–1604.
- Weinberger, C. R., Aubry, S., Lee, S.-W., Cai, W., 2009. Dislocation dynamics simulations in a cylinder. *IOP Conference Series: Materials Science and Engineering* 3 (1), 012007.
- Weingarten, N. S., Chung, P. W., 2013. *a*-Type edge dislocation mobility in wurtzite GaN using molecular dynamics. *Scripta Materialia* 82 (4), 311–314.
- Weygand, D., Friedman, L. H., Giessen, E. V. d., Needleman, A., 2002. Aspects of boundary-value problem solutions with three-dimensional dislocation dynamics. *Modelling and Simulation in Materials Science and Engineering* 10 (4), 437.
- Willis, J. R., 1970. Stress fields produced by dislocations in anisotropic media. *Philosophical Magazine* 21 (173), 931–949.
- Wright, A. F., 1997. Elastic properties of zinc-blende and wurtzite AlN, GaN, and InN. *Journal of Applied Physics* 82 (6), 2833–2839.
- Yasin, H., Zbib, H. M., Khaleel, M. A., 2001. Size and boundary effects in discrete dislocation dynamics: coupling with continuum finite element. *Materials Science and Engineering: A* 309-310, 294–299.
- Yin, J., Barnett, D. M., Cai, W., 2010. Efficient computation of forces on dislocation segments in anisotropic elasticity. *Modelling and Simulation in Materials Science and Engineering* 18 (4), 045013.
- Yoffe, E. H., 1961. A dislocation at a free surface. *Philosophical Magazine* 6 (69), 1147–1155.
- Yonenaga, I., 2003. High-temperature strength of bulk single crystals of III-V nitrides. *Journal of Materials Science: Materials in Electronics* 14 (5), 279–281.
- Yonenaga, I., Itoh, S., Goto, T., 2003. Dislocation mobility and photoluminescence of plastically deformed GaN. *Physica B: Condensed Matter* 340-342, 484–487.
- Yonenaga, I., Ohno, Y., Taishi, T., Tokumoto, Y., 2009. Recent knowledge of strength and dislocation mobility in wide band-gap semiconductors. *Physica B: Condensed Matter* 404 (23-24), 4999–5001.

- Zbib, H. M., Díaz de la Rubia, T., 2002. A Multiscale Model of Plasticity. *International Journal of Plasticity* 18 (9), 1133–1163.
- Zbib, H. M., Díaz de la Rubia, T., Bulatov, V. V., 2001. A Multiscale Model of Plasticity Based on Discrete Dislocation Dynamics. *Journal of Engineering Materials and Technology* 124 (1), 78–87.
- Zhu, D., Wallis, D. J., Humphreys, C. J., 2013. Prospects of III-nitride optoelectronics grown on Si. *Reports on Progress in Physics* 76 (10), 106501.